J Sol-Gel Sci Technol (2015) 74:765–773
DOI 10.1007/s10971-015-3661-0

ORIGINAL PAPER

Comparison of optical and structural properties of Cu doped and Cu/Zr co-doped TiO_2 nanopowders calcined at various temperatures

Nasrollah Najibi Ilkhechi · Behzad Koozegar Kaleji · Esmaeil Salahi · Navid Hosseinabadi

Received: 21 September 2014 / Accepted: 9 February 2015 / Published online: 26 February 2015

Abstract TiO_2 nanopowders doped with Cu and Zr were prepared via process-controlled sol–gel method. The effects of Zr and Cu doping on the structural and photocatalytic properties of synthesized nanopowders have been studied by X-ray diffraction (XRD), scanning electron microscope, transmission electron microscope, FTIR, and UV–Vis absorption spectroscopy. XRD results suggested that adding dopants has a great effect on crystallinity and particle size of TiO_2. Titania rutile phase formation was inhibited by Zr^{4+} and promoted by Cu^{2+} doping. The photocatalytic activity was evaluated by degradation kinetics of aqueous methyl orange under visible spectra radiation. The results showed that the photocatalytic activity of the 15 % Zr-doped TiO_2 nanopowder has a larger degradation efficiency than 5 % Cu-doped and pure TiO_2 under visible light.

Keywords TiO_2 · Nanopowder · Sol–gel · Photocatalytic activity · Zr and Cu dopant

N. N. Ilkhechi (✉) · B. K. Kaleji
Department of Materials Engineering, Faculty of Engineering, Malayer University, P.O. Box 65719-95863, Malayer, Iran
e-mail: nasernajibi@gmail.com

B. K. Kaleji
e-mail: bkaleji@yahoo.com; b.kaleji@malayeru.ac.ir

E. Salahi
Material and Energy Research Center (MERC) Center, P.O. Box 31878-316, Karaj, Iran

N. Hosseinabadi
Department of Materials Engineering, Faculty of Chemical and Materials Engineering, Shiraz Branch, Islamic Azad University, Shiraz, Iran

1 Introduction

Titanium dioxide has been widely used in the field of pollutant degradation and environment protection since photocatalytic function of titania was discovered in 1972 [1, 2].

The titanium dioxide has the advantage of not only high photocatalytic activity, but also good acid resistance, low cost, and no toxicity, which makes the titanium dioxide one of the best photocatalytic agents [3, 4].

Among various phases of titania, anatase shows better photocatalytic activity with anti-bacterial performance [5–9]. A stable anatase phase up to the sintering temperature of the ceramic substrates is the most desirable property for applications on anti-bacterial self-cleaning building materials (e.g., bathroom tile, sanitary wares.) These applications require high-purity titania with a definite phase composition. The production of highly photoactive material with high-temperature anatase phase stability is one of the key challenges in smart coating technology [10–12]. For this purpose, doping or combining TiO_2 with various metals (Au, Pt, Ir) or nonmetal ions has been considered [13, 14]. The metal ions that are found to inhibit the anatase-to-rutile phase transformation are Si, Zr [15–17], W, Nb, Ta, Cr [18], while the metal ions that are reported to promote the phase transformation are Ni, Co, Mn, Fe, Cu [19], V [18], and Ag [20]. Numerous reports are available regarding the shift of wavelength corresponding to the onset of absorption from UV to visible light in TiO_2 as the result of doping with cationic or anionic dopants. Anionic dopants such as nitrogen, sulfur, carbon, and fluorine lead to narrower band gaps for TiO_2, which results in visible light absorption and improved photocatalytic activity [21–23].

Sensitization of Cu-doped TiO_2 with eosin improved the photocatalytic activity for water splitting under visible light

irradiation [24]. In this case, CuO not only brings about the charge separation but also provides active sites for water splitting. Doping of TiO_2 with 0.1 % Nd and impregnation with Pt produced enhanced photocatalytic activity for water splitting due to the prevention of phase transformation of TiO_2 from anatase to rutile and inhibition of particle growth [25].

Some recent studies have revealed that the oxygen-deficient sites play a crucial role in the visible light-induced photocatalytic activity of TiO_2. Ihara et al. [26] have reported that the low-temperature H_2 plasma-treated TiO_2 and nitrogen-doped TiO_2 [27] showed visible light photocatalytic activity due to the presence of oxygen-deficient sites.

Prokes et al. [28] have proposed that the visible light absorption of titanium oxynitride is due to the oxygen hole center created during the surface modification process by nitrogen near the surface of the nanocolloid. The visible light photocatalytic activity observed due to the oxygen vacancies in TiO_2 is found to decrease after an optimum value.

The mixed oxides of TiO_2–ZrO_2 have been extensively used as catalysts and catalyst supports for a wide variety of reactions. In addition to catalytic applications, these mixed oxides have also been employed for various other purposes such as photoconductive thin films and gas sensors in fuel cell and ceramic technologies. The TiO_2–ZrO_2 composite oxides exhibit high surface area, profound surface acid–base properties, a high thermal stability, and strong mechanical strength applications [29–33].

In our previous research, we studied the effect of doping Si (up to 20 mol%) and Zr (up to 20 mol%) on photocatalytic behavior of titania based nanopowders at high temperature. We found that 20 % of Si and 15 mol% Zr shows the most significant improvement on photocatalytic behavior of TiO_2 under visible irradiation and also, we checked stability of anatase phase up to 1000 °C [16].

In this paper, the TiO_2 nanopowder, doped with 15 mol% Zr and 5 mol% Cu, was prepared by sol–gel method. The effect of the dopant cations and calcination temperature on the structure and optical properties was studied in a systematic way. The efficiency of these samples as photocatalysts for the degradation of methyl orange (MO), as organic compound model, under visible light, was investigated.

2 Experimental procedures

2.1 Preparation of the pure and doped titania nanopowders

The preparation of precursor solution for Zr- and Cu-doped TiO_2 nanopowder is described as follows: TiO_2, ZrO_2, and CuO sols were prepared, separately. Titanium (IV) butoxide [TBT = $Ti(OC_4H_9)_4$, Aldrich] was selected as titanium source. 10 ml ethanol (EtOH, Merck) and 4 ml ethyl acetoacetate (EAcAc is as a sol stabilizer during preparation of sol) were mixed, and then, 4 ml TBT was added by the rate of 1 ml/min to the mixture at the ambient temperature (25 °C). The solution was continuously stirred for 1 h, followed by dropping of HNO_3 as catalyst to the solution until pH 3. Deionized water was added to the solution slowly to initiate hydrolysis process. Solution was kept for 24 h in order to complete all reactions. The chemical composition of the alkoxide solution was TBT:H_2O:HNO_3:EAcAc:EtOH = 1:8:3:0.05:5 in volume ratio. In order to prepare ZrO_2 and CuO sol, zirconyl nitrate hydrate [$ZrO(NO_3)\cdot 2H_2O$, Aldrich], and [$Cu(NO_3)_2\cdot 3H_2O$, Merck] were dissolved in EtOH with volume ratio of $ZrO(NO_3)\cdot 2H_2O$:EtOH = 1:20 and $Cu(NO_3)_2\cdot 3H_2O$:EtOH = 1:6 at ambient temperature with continuous stirring. Cu was doped 10 min after Zr doping under continuous stirring at room temperature. Then, mixtures of TiO_2, ZrO_2, and CuO sols were made with different mol ratios at the ambient temperature. The mol ratios of Zr and Cu in mixtures were 5 and 15 mol%, respectively. The formed gel was dried at 100 °C for 60 min. Samples finally, calcined at desired temperatures (500, 600, 700, 800, 900, 1000 °C) for 2 h.

2.2 Characterization methods

Samples were recorded using X-ray diffraction (XRD) analysis (Philips, MPD-XPERT, λ:Cu $K_\alpha = 0.154$ nm). The samples were scanned in the 2θ ranging of 20°–60°. The average crystallite size of nanopowders (d) was determined from the XRD patterns, according to the Scherrer equation [16]

$$d = k\lambda/\beta\cos\theta \quad (1)$$

where k is a constant (shape factor, about 0.9), λ the X-ray wavelength (0.154 nm), β the full width at half maximum (FWHM) of the diffraction peak, and θ is the diffraction angle. The values of β and θ of anatase and rutile phases were taken from anatase (1 0 1) and rutile (1 1 0) plane diffraction lines, respectively. The amount of rutile in the samples was calculated using the following equation [16]

$$X_R = (1 + 0.8(I_A/I_R))^{-1} \quad (2)$$

where X_R is the mass fraction of rutile in the samples, and I_A and I_R are the X-ray integrated intensities of (1 0 1) reflection of the anatase and (1 1 0) reflection of rutile, respectively. The diffraction peaks of crystal planes (101), (200), and (105) of anatase phase in XRD patterns were selected to determine the lattice parameters of the TiO_2 and doped TiO_2 nanopowders. The lattice parameters were obtained by using the Eq. 3 [16]

$$(\text{Bragg's law}) : 2d_{(h\,k\,l)}\sin\theta = \lambda \quad (3)$$

$$(1/d_{h\,k\,l})^2 = (h/a)^2 + (k/b)^2 + (l/c)^2 \quad (4)$$

where $d_{(h\ k\ l)}$ is the distance between the crystal planes of (h k l); λ is the wavelength of X-ray used in the experiment; θ is the diffraction angle of the crystal plane (h k l); h k l is the crystal plane index; and a, b, and c are lattice parameters (in anatase form, $a = b \neq c$).

Morphology of the nanopowder was observed using scanning electron microscope (SEM, XL30 Series) with an accelerating voltage of 10–30 kV. Transmission electron microscope (TEM) imaging was carried out using Zeiss-EM10C-80 kV instrument. FTIR absorption spectra were measured over the range of 4000–400 cm^{-1} at room temperature.

Nitrogen adsorption isotherms were measured at 77 K using a N_2 adsorption analyzer (Micromeritics, ASAP 2020). The Brunauer, Emmett, and Teller (BET) model was used to estimate the surface area of the samples according to the N_2 adsorption data.

2.3 Photocatalytic activity measurement

The photocatalytic activities of the catalyst were evaluated by the degradation of organic dyes including MO under visible light irradiation. Typically, approximately 0.08 g of catalyst was added to 50 mL of aqueous MO solutions. Prior to irradiation, the suspensions were stirred in the dark for 1 h to obtain a colloidal solution. The photocatalytic experiment was conducted at room temperature in a cylindrical glass vessel equipped with magnetic stirrer under an visible light positioned horizontally and 10 cm above the colloid surface. The glass vessel was illuminated by 150 W lamps (halogen, made in Iran). The entire arrangement was placed in a box sealed with aluminum foil to avoid the passage of light into the box. Prior to irradiation, the colloidal solutions were magnetically stirred in the dark to establish the absorption equilibrium of MO in solution. Under ambient conditions and stirring, the solution in the glass vessel was exposed to visible light. Then, the solutions were the irradiated under visible light with constant stirring rate of 450 rpm. After 40 min irradiation, 5 ml of supernatants were taken from the suspension by a syringe filter unit to scan the UV–Vis absorption spectrum. The UV–Vis absorption spectra of samples were measured between 200 and 1000 nm UV–Vis spectrophotometer.

The extent of the MO decomposition was determined by measuring the value of the absorbance value at 478 nm [max absorption of (MO)] using a UV–Vis spectrometer. The degradation rate [η (%)] of MO was calculated by the following formula:

$$\eta\,(\%) = (A_0 - A_t)/A_0 \times 100 \quad (5)$$

where A_0 and A_t represent the initial equilibrium absorption and reaction concentration of reactant at 478 nm, respectively [16].

3 Results and discussion

3.1 X-ray diffraction studies of the nanopowders

Figure 1 shows the XRD patterns of TiO_2 (T), T–5 % Cu (TC), and T–5 % Cu–15 % Zr (TCZ) samples calcined at 500 °C for 2 h. XRD peak at 25.3° corresponds to characteristic peak of (101) plane in anatase and at 27.8° corresponds to characteristic peak of (1 1 0) of rutile in nanopowders. According to the XRD pattern (Fig. 1), the pure and doped TiO_2 was crystallized in anatase phase. Also, by comparing the relative intensity of the diffraction peaks, it can be seen that the intensity of (101) plane decreased with changing peak position (2θ) to lower degrees with doping. Also, the diffraction peaks at 2θ angle 37.63, 61, 47.93, 53.98, and 62.64 correspond to diffraction from planes (103), (200), (105), and (213), respectively, of anatase phase at temperature 500 °C decreased or removed. The calculated crystallite sizes of anatase, calculated by Scherrer formula, are reported in Table 1. The crystallite size of TiO_2 powder depends on the dopant. For pure TiO_2, the anatase crystallite size decreased significantly with the presence of Cu- and Zr-co-doped relative Cu doped. The decrease in crystallite size can be attributed to the presence of Cu–O–Ti and Zr–O–Ti in the Cu- and Zr-co-doped TiO_2 nanopowder which inhibits the growth of crystal grains [16]. Also, the lattice parameters, surface area, and cell volume of the TiO_2 and doped TiO_2 nanopowders are

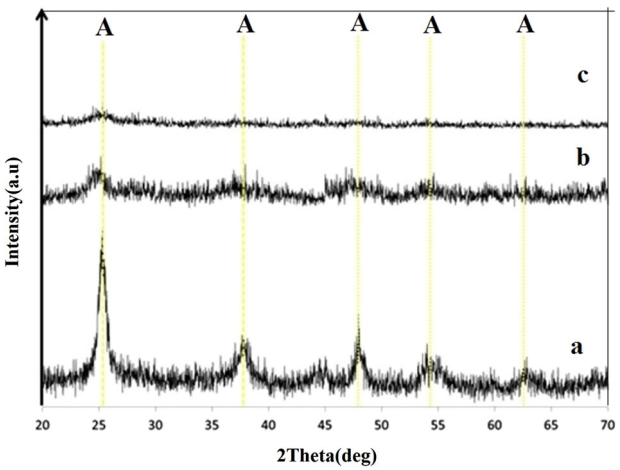

Fig. 1 XRD spectra of the pure and doping TiO_2 nanopowders at 500 °C **a** TiO_2 (T), **b** TiO_2–5 % Cu (TC), and **c** TiO_2–5 % Cu–15 % Zr (TCZ)

Table 1 Characterization of pure and doped TiO_2 (TC, TCZ) at temperature 500 °C

Sample	A (%)	R (%)	Crystallite size (nm)		$a = b$ (Å)	c (Å)	Cell volume (Å)^3	S (m^2/g)
			d_A	d_R				
TiO_2 (T)	100	–	9.47	–	3.767	8.944	126.917	183.2
T–5 % Cu	100	–	8.35	–	3.798	12.086	174.331	208.7
T–5 % Cu–15 % Zr	100	–	7.45	–	3.821	12.863	187.80	233.4

summarized in Table 1. It is obvious that the lattice parameters, surface area, and cell volume of the doped TiO_2 nanopowders increase with increasing amount of Zr and Cu substitution for Ti^{4+} in titania lattice.

The XRD patterns of Cu-doped TiO_2 nanopowders calcined at different temperatures are shown in Fig. 2. As calcination temperature increased, broad peaks detected at lower temperatures became sharper, indicating the evolution of a crystalline anatase phase until 700 °C, and then, anatase phase transformed to the rutile phase. Samples heated at 800–1000 °C crystallized only in rutile phase. Results showed that the addition of Cu has a promoting effect on the transformation of anatase to rutile crystalline phase [16, 24]. All the samples were identified as the mixture polymorphs of anatase (JCPDS: No. 21-1272) and rutile (JCPDS: No. 21-1276), without any impurity phase, which suggests the incorporation of Cu^{2+} in TiO_2 lattice. Also, since the ionic radius of Cu^{+2} ion (0.58 Å, CN: 4) is closer to Ti^{4+} ion (0.66 Å, CN: 6) in TiO_2, it is expected that the Cu^{+2} ions will replace lattice Ti^{4+} ions and thus occupy lattice Ti^{4+} positions during doping process.

It is clear from Table 2 that the crystallite size increased but the surface area decreased with an increase of the calcination temperatures for anatase (600, 700 °C) and rutile (800–1000 °C) nanoparticles. The size of the anatase crystallites increased from 8.35 to 10.19 nm when the temperature is raised to 600 °C. As the temperature elevates from 500 to 1000 °C, the crystallite size of the powder greatly increases to ~32.36 nm. Minimum surface area of 44.1 m^2/g was measured. It is common that the surface area decreases with the elevating temperature due to the degree of crystallinity. In the samples calcined at 1000 °C, higher crystalline structure led to a decrease in surface area.

The XRD patterns of 15 mol% Zr- and 5 mol% Cu-doped TiO_2 nanopowders calcined at different temperatures are shown in Fig. 3, anatase appeared as the main phase, and rutile crystallization was inhibited by Zr^{4+} doping up to 800 °C like Cu^{2+} doping (Fig. 2). Also, at 800 °C the percent of rutile phase found to be 26 % and samples heated at 900–1000 °C showed only the rutile phase. The results showed that the addition of 15 mol% Zr into T–5 % Cu has an inhibition effect on anatase-to-rutile crystalline phase transformation at 800 °C [16, 34]. The

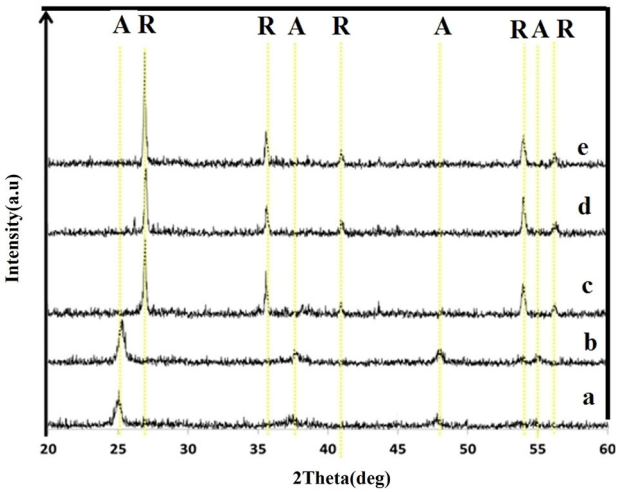

Fig. 2 XRD spectra of the T–5 % Cu (TC) nanopowders at different temperatures **a** 600 °C, **b** 700 °C, **c** 800 °C, **d** 900 °C, and **e** 1000 °C

crystal characteristics of all samples are reported at Table 3. It is obvious that the lattice parameters and surface area of the Zr- and Cu-co-doped TiO_2 are higher than Cu-doped nanopowders.

Average anatase crystallite sizes decreased from T–5 % Cu, to Zr-doped T–5 % Cu. It showed that the Zr dopants can inhibit the anatase grain growth. The Zr^{4+} radius (0.72 Å) is slightly bigger than Ti^{4+} radius (0.66 Å), which means Zr^{4+} induces slight stress in TiO_2 lattice, which may hinder the growth of the TiO_2 crystallites.

3.2 FTIR analysis of pure and doped TiO_2 nanopowders

Figure 4 shows the FTIR spectrum of the nanocrystalline TiO_2 powder calcined at 500 °C in the range of 400–4000 cm^{-1}. Metal oxides generally give absorption bands in fingerprint region below 1000 cm^{-1} arising from inter-atomic vibrations.

The infrared spectra (Fig. 4) of pure and doped TiO_2 exhibited the following bands:

1. 3442.27 and 3332.02 cm^{-1} due to intermolecular structure and the O–H band [35]
2. 511.02 and 511.04 cm^{-1} which can be attributed to the Ti–O stretching and Ti–O–Ti binding stretching modes [36]

Table 2 Characterization of 5 % Cu-doped TiO_2 (TC) at different temperature

Calcination temperature (°C)	A (%)	R (%)	Crystallite size (nm)		$a = b$ (Å)	c (Å)	Cell volume (Å)^3	S (m^2/g)
			d_A	d_R				
600	100	–	10.19	–	3.796	9.431	136.009	150.9
700	100	–	13.89	–	3.770	6.019	85.547	110.7
800	–	100	–	17.93	4.679	2.997	65.613	79.6
900	–	100	–	24.50	4.681	2.991	65.538	58.3
1000	–	100	–	32.36	4.664	3.000	65.258	44.1

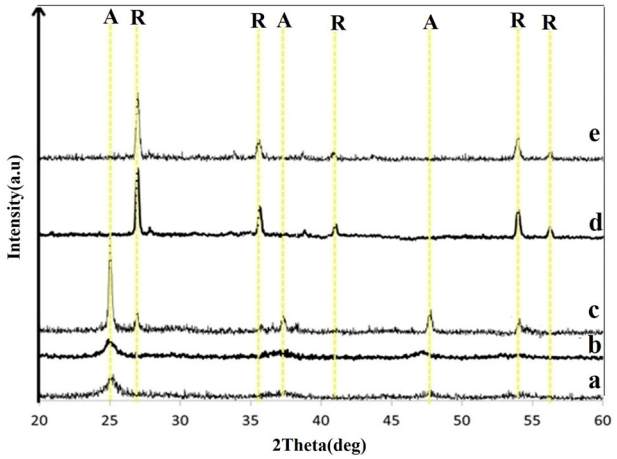

Fig. 3 XRD spectra of the TCZ nanopowders at different temperatures **a** 600 °C, **b** 700 °C, **c** 800 °C, **d** 900 °C, and **e** 1000 °C

3. 472.02 cm^{-1} which can be attributed to the vibrations of Cu–O [35]
4. Band around 506.39 cm^{-1} corresponds to Cu–O–Ti or Zr–O–Ti [36, 37]

3.3 Photocatalytic evaluation

The reported optical band gap (E_g) in Fig. 5 was calculated using the UV–Vis spectra formula [34]:

$$\alpha h\upsilon = A\left(h\upsilon - E_g\right)^n \quad (6)$$

where $h\upsilon$ is the photon energy, and A and n are constants. For allowed direct transition, $n = 1/2$; for direct forbidden transition, n = 3/2; and for indirect allowed transition, $n = 2$. The optical band gap energy (E_g) is found by extrapolating the straight line portion of $(\alpha h\upsilon)^{1/2}$ with the abscissa axis ($h\upsilon$) in the vicinity of the fundamental optical transition for pure and doped nanopowders. It can be seen from Tauc plots (Fig. 5) that band gap of pure TiO_2 nanoparticles is 3.12 eV. Also, the values of band gap calculated from Tauc plots were found to be 2.65 and 2.42 eV for TC and TCZ, respectively, at 500 °C. It indicates a decrease in the energy band gap (inset in Fig. 5). It has been reported that metal doping could form a dopant energy level within the band gap of TiO_2 [16, 34, 37–39]. The largest reduction band gap is observed for co-doped catalysts of 5 mol% of Cu- and 15 mol% of Zr-co-doped TiO_2. This large reduction band gap may be attributed to those impurities incorporated into the host (TiO_2) structure, which create extra energy levels within the band gap. Due to the creation of extra energy level within the band gap, Fermi energy will shift away from the center of the band gap toward valence band, since both metals create P-type semiconductor [40].

The band gap energy of TC and TCZ calcined at 500–1000 °C are shown in Table 4. Band gap of samples decreased with the increase of the calcination temperature. A significant decrease can be assigned to absorption of light caused by the excitation of electrons from the valence band to the conduction band of titania. The band gap of the

Table 3 Characterization of T–5 % Cu–15 % Zr (TCZ) at different temperature

Calcination temperature (°C)	A (%)	R (%)	Crystallite size (nm)		$a = b$ (Å)	c (Å)	Cell volume (Å)^3	S (m^2/g)
			d_A	d_R				
600	100	–	9.82	–	3.808	10.000	145.001	156.6
700	100	–	12.09	–	3.834	11.442	168.192	127.2
800	74	26	17.81	22.92	3.802	9.972	144.203	86.3
900	–	100	–	23.26	4.542	2.955	60.960	61.4
1000	–	100	–	29.92	4.666	3.001	65.331	47.7

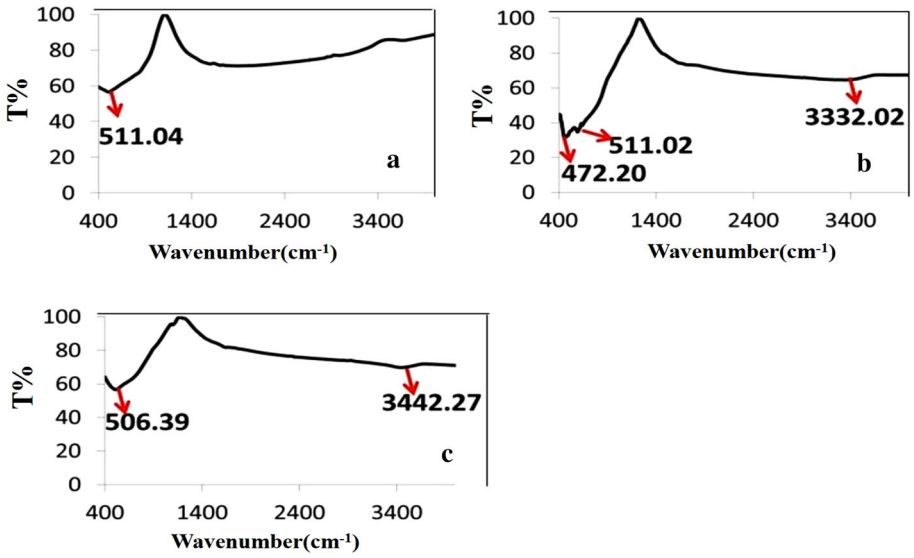

Fig. 4 FTIR spectra of pure and doped TiO_2 nanoparticles calcined at temperatures 500 °C **a** T, **b** TC, and **c** TCZ

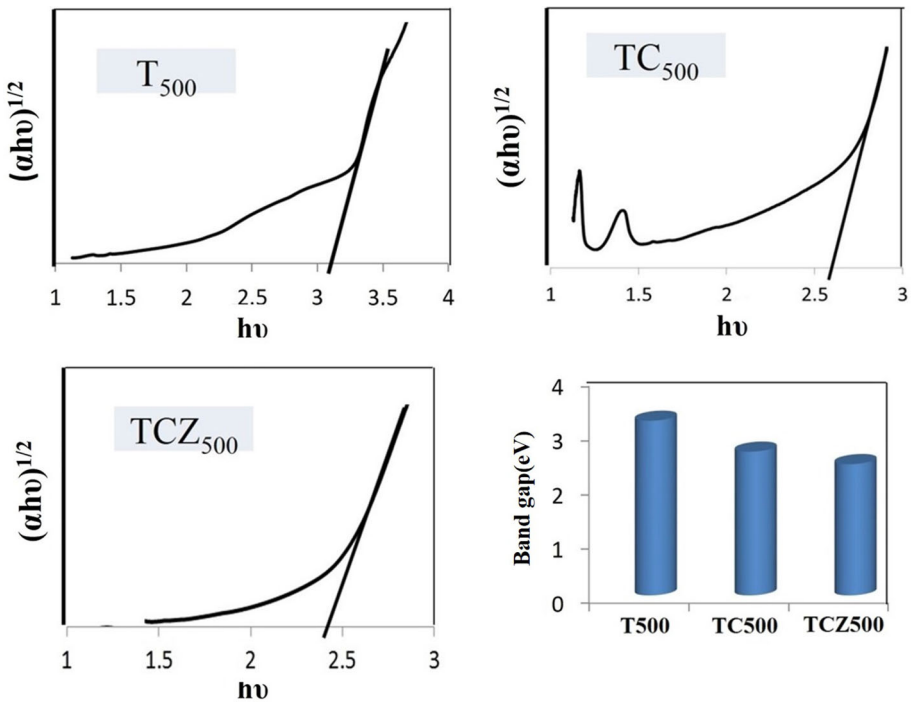

Fig. 5 Tauc plots of T, T–5 % Cu (TC) and T–5 % Cu–15 % Zr (TCZ) nanopowders calcined at 500 °C

TC and TCZ had decreased to 2 and 2.12 eV with increasing temperature up to 1000 °C.

Figure 6 shows the results of photocatalytic decomposition of MO solution caused by degradation of MO in contact with nanopowders with Zr and Cu dopants at different calcination temperatures. According to Fig. 6, photocatalytic activity of TiO_2 nanopowders after 40 min under the visible irradiation is increased, which suggests that the doping enhances the photocatalytic activity of

Table 4 Band gap energy of TC and TCZ at different temperature

Sample temperature (°C)	TC (eV)	TCZ (eV)
600	2.51	2.32
700	2.43	2.28
800	2.30	2.20
900	2.26	2.16
1000	2.12	2

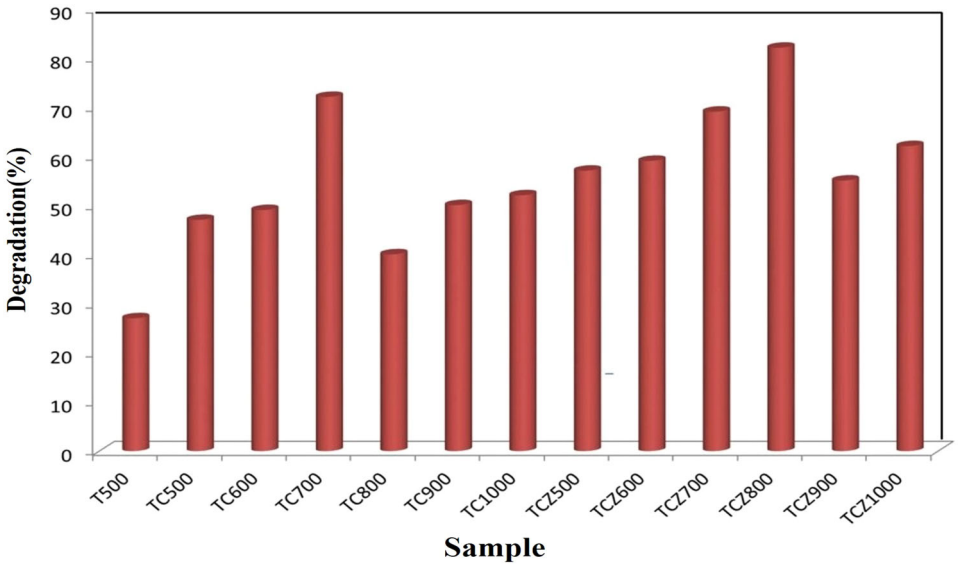

Fig. 6 Photocatalytic degradation of MO determined by pure and doped TiO_2 nanopowders after 40 min visible irradiation at different temperature

TiO_2. This enhanced photocatalytic activity is due to suppressed recombination of photogenerated electrons and holes [41].

Figure 6 shows that the near 72 % of MO was decomposed at the presence of T–5 % Cu (700 °C) after visible irradiation for 40 min, while the values in the presence of T–5 % Cu–15 % Zr (800 °C) and T (500 °C) are 84 and 27 %, respectively. The highest photodegradation of MO caused by TCZ sample calcined at a temperature of 800 °C with anatase and rutile mixed structure.

The calcined samples at 900 and 1000 °C have rutile structure and gave lower degradation efficiency compared to the samples calcined at lower temperatures. Our results are in good agreement with those obtained in a previous study [16]. Some studies indicated that the photocatalytic activity of TiO_2 catalysts depends strongly on two factors: adsorption behavior and the separation efficiency of electron–hole pairs [42]. On the other hand, the results showed that the specific surface areas of the catalysts increased from 183.2 m^2/g for undoped TiO_2 to 208.7 m^2/g for Cu-doped TiO_2 and 233.4 m^2/g for Cu- and Zr-co-doped TiO_2 (shown in Table 1).

The larger specific surface area of doped TiO_2 catalysts would be beneficial to achieve better adsorption and degradation of MO in aqueous suspension. Therefore, the presence of dopant seems to be helpful for the photocatalytic activity. According to Fig. 6 and Table 1, the photocatalytic reactivity of doped TiO_2 nanopowders is higher than that of undoped TiO_2, which is consistent with the larger specific surface area of doped TiO_2 than undoped TiO_2.

3.4 SEM–EDX and TEM analysis of pure and doped TiO_2 nanopowders

Figure 7 represents the SEM images of pure ad doped TiO_2 sample calcined at 500 °C. The morphologies of the powders are quite similar. Pure and Cu-doped TiO_2 nanopowders calcined at 500 °C exhibited similar spherical particles with a wide diameter range from 100 to 300 nm.

However, a precise study of the images can reveal the aggregation of crystallites. Also, it can be observed that the aggregation of particles in the doped samples than the undoped TiO_2. Besides SEM analysis, EDX analysis was performed on powders in order to investigate the elemental structure. The analyses revealed the existence of Ti as the main element. The EDX data of doped TiO_2 in Fig. 8a, b show two peaks around 4.5 keV.

The intense peaks are assigned to the bulk TiO_2 and the less intense one to the surface TiO_2. The peaks of Cu and Zr are distinct in Fig. 8 at 0–2.6 keV (Fig. 8a, b). The less intense peak is assigned to dopant in the TiO_2 lattices. These results confirmed the existence of cations in the solid catalysts.

Figure 9 shows the TEM micrographs of pure and doped TiO_2 particles calcined at 500 °C. It could be found that the pure TiO_2 particles appeared as uniform and agglomerated shapes. The doped sample had better

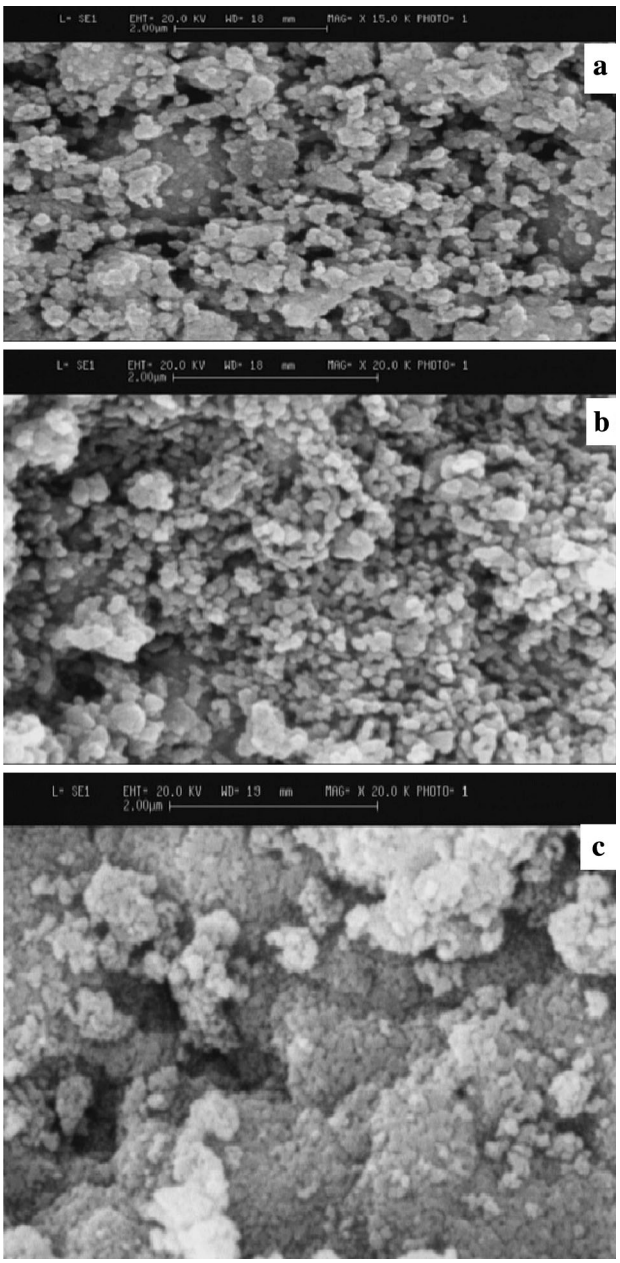

Fig. 7 SEM-EDX images of pure and doped TiO_2 (TC, TCZ) nanopowders calcinations at 500 °C **a** T, **b** TC, **c** TCZ, **d** EDX–TC, and **d** EDX–TCZ nanopowders

dispersibility than pure TiO_2, and the particle size was smaller (Fig. 9b, c). Additionally, the Cu- and Zr-co-doped products were more and more dispersed (Fig. 9c). The Cu–Zr-co-doped TiO_2 nanocrystallite prepared in nonaqueous system possessed little hydroxyl group comparing to that synthesized in aqueous system; thus,

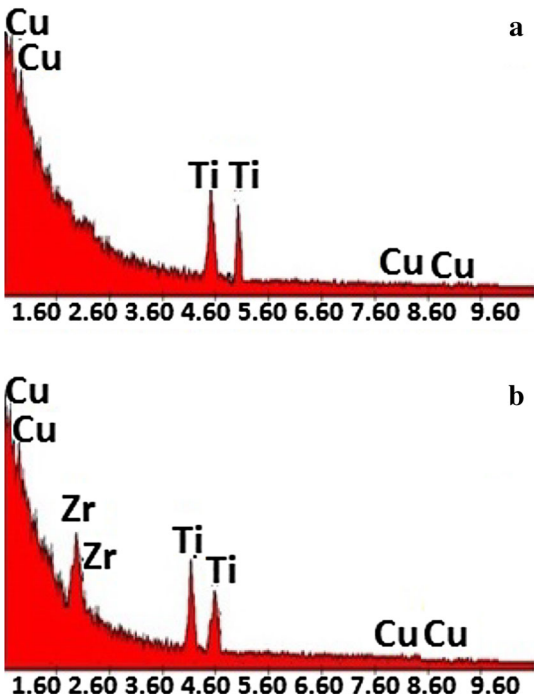

Fig. 8 EDX images of doped TiO_2 (TC, TCZ) nanopowders calcinations at 500 °C **a** TC, **b** TCZ

aggregation among nanocrystallites could decrease during heating treatment. On the other hand, doped Cu and Zr could prevent TiO_2 nanocrystallite from aggregating. Therefore, the particle size was smaller, and particle dispersibility was higher than undoped TiO_2.

4 Conclusion

In this research, Zr- and Cu-co-doped TiO_2 nanopowders with photocatalytic activities have been prepared via sol–gel method. The anatase to rutile phase transformation was promoted by Cu^{+2} doping but inhibited by Zr^{4+} doping. The photocatalytic activity of the doped nanopowders is higher than that of pure TiO_2 nanopowders. Zr^{4+} and Cu^{2+} substitution for Ti^{4+} in the titania lattice results in a decrease in the rate of photogenerated electron–hole recombination that is responsible for the enhancement in photocatalytic degradation rate. Photocatalytic activity of the doped nanopowders under visible irradiation was improved compared to undoped TiO_2 nanopowders. Under visible irradiation, T–5 % Cu–15 % Zr has larger decomposition ability than T–5 % Cu.

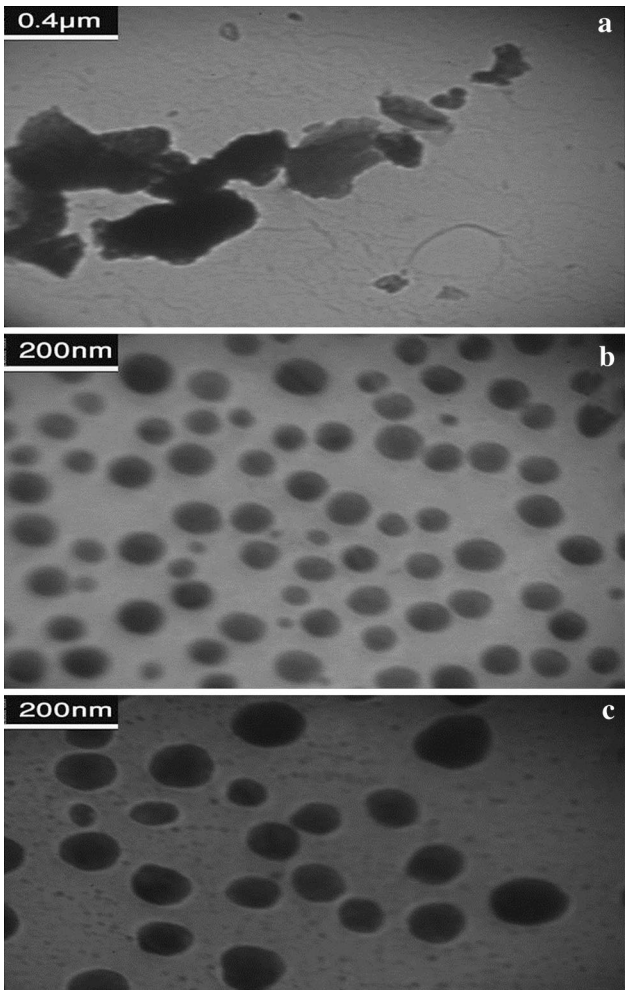

Fig. 9 TEM micrograph of T, TC, and TCZ calcined at 500 °C **a** T, **b** TC, and **c** TCZ

References

1. Fujishima A, Honda K (1972) Nature 238:37–38
2. Samuneva B, Kozhukharov V (1993) Mater Sci 28:2353–2360
3. Wang CY, Liu CY, Shen T (1997) J Photochem Photobiol A Chem 109:65–70
4. Palmer FL, Eggins BR (2002) J Photochem Photobiol 148:137–143
5. Yang SW, Gao L (2005) J Am Ceram Soc 88:968–970
6. Karakitsou KE, Verykios XE (1993) J Phys Chem B 97:1184–1189
7. Hu C, Lan Y, Hu X, Wang A (2006) J Phys Chem B 110:4066–4072
8. Sakatani Y, Grosso D, Nicole L, Boissiere C, Illia S, Sanchez C (2007) J Mater Chem 16:77–82
9. Fujishima A, Rao TN, Tryk DA (2001) J Photochem Photobiol C Photochem Rev 1:1–21
10. Parkin IP, Palgrave RG (2005) J Mater Chem 15:1689–1695
11. Mills A, Lee SK (2006) J Photochem Photobiol A Chem 182:181–186
12. Zanderna AW, Rao CNR, Honig JM (1958) Trans Faraday Soc 54:1069–1073
13. Subramanian V, Wolf E, Kamat PV (2001) J Phys Chem B 105:11439–11446
14. Rajeshwar K, Tacconi NR, Chenthamarakshan CR (2001) Chem Mater 13:2765–2782
15. Okada K, Yamamoto N, Kameshima Y, Yasumori A, MacKenzie K (2001) J Am Ceram Soc 84:1591–1596
16. Ilkhechi NN, Kaleji KB (2014) J Sol-Gel Sci Technol 69:351–356
17. Hanaor DAH, Sorrell CC (2011) J Mater Sci 46:855–874
18. Ohtsuka Y, Fujiki Y, Suzuki Y (1982) J Jpn Assoc Mineral Petrol Econ Geol 77:17–124
19. Iida Y, Ozaki S (1961) J Am Ceram Soc 44:120–127
20. Chao HE, Yun YU, Xingfang HU, Larbot A (2003) J Eur Ceram Soc 23:1457–1464
21. Yin S, Ihara K, Aita Y, Komatsu M, Sato T (2006) J Photochem Photobiol A Chem 179:105–114
22. Yin S, Yamaki H, Komatsu M, Zhang Q, Wang J, Tang Q (2003) J Mater Chem 13:2996–3001
23. Colon G, Hidalgo MC, Munuera G, Ferino I, Cutrufello MG, Navio JA (2006) Appl Catal B Environ 63:45–59
24. Jin Z, Zhang X, Li Y, Li S, Lu G (2007) Catal Commun 8:1267–1273
25. Cuiying H, Wansheng Y, Ligin D, Zhibin L, Zhengang S, Lancui Z (2006) Chin J Catal 27:203–209
26. Ihara T, Miyoshi M, Ando M, Sugihara S, Iriyama Y (2001) J Mater Sci 36:4201–4207
27. Ihara T, Miyoshi M, Iriyana Y, Matsumoto O, Sugihara S (2003) Appl Catal B Environ 42:403–409
28. Prokes SM, Gole JL, Chen X, Burda C, Carlos WE (2005) Adv Funct Mater 15:161–167
29. Sham EL, Aranda MAG, Farfan-Torres EM, Gottifredi JC (1998) J Solid State Chem 139:225–232
30. Liping L, Yonggang S, Yao Z, Dong W, Yuhan S (2007) Thin Solid Films 515:7765–7771
31. Cosentino IC, Muccillo ENS, Muccillo R (2003) Sens Actuator B 96:677–683
32. Azough F, Freer R, Petzelt J (1993) J Mater Sci 28:2273–2276
33. Manŕıquez ME, López T, Gómez R, Navarrete J (2004) J Mol Catal A Chem 220:229–237
34. Kapusuz D, Park J, Ozturk A (2013) J Phys Chem Solids 74:1026–1031
35. Ilkhechi NN, Koozegar-Kaleji B, Dousi F (2015) Opt Quant Electron 47:633–642
36. Rogéria RG, Younes M, Mohamed A, Sidney JLR (1999) Mater Res 2:11–15
37. Hussain ST, Mazhar M, Siddiqa M, Javid H, Siddiqa M (2012) Catal J 5:21–30
38. Kaleji KB, Sarraf-Mamoory R, Nakata N, Fujishima A (2011) J Sol-Gel Sci Technol 60(2):99–107
39. Adriana Z (2008) Recent Pat Eng 2:157–164
40. Akpan UG, Hameed BH (2010) Appl Catal A 375:1–11
41. Ramesh T, Saravanamuthu V, Shik M (2008) Korean J Chem Eng 25(1):64–72
42. Beydoun D, Amal R, Low G, McEvoy S (1999) J Nanopart Res 1:439–458